Soft Matter

PAPER

Cite this: *Soft Matter*, 2019, **15**, 3008

Support of modified Archimedes' law theory in granular media

Yajie Feng,[a] Raphael Blumenfeld[bc] and Caishan Liu*[a]

We study the resistance force of cylindrical objects penetrating quasi-statically into granular media experimentally and numerically. Simulations are validated against experiments. In contrast to previous studies, we find in both experiments and simulations that the force–depth relation consists of three regimes, rather than just two: transient and steady-state. The three regimes are driven by different dynamics: an initial matter compression, a developing stagnant zone, and an increase in steady-state force with a fully developed stagnant zone. By simulations, we explored the effects of a wide range of parameters on the penetration dynamics. We find that the initial packing fraction, the inter-granular sliding friction coefficient, and the grain shape (aspect ratio) have a significant effect on the gradient K_ϕ of the force–depth relation in the steady-state regime, while the rolling friction coefficient noticeably affects only the initial compression regime. Conversely, K_ϕ is not sensitive to the following grain properties: size, size distribution, shear modulus, density, and coefficient of restitution. From the stress fields observed in the simulations, we determine the internal friction angles ϕ, using the Mohr–Coulomb yield criterion, and use these results to test the recently-proposed modified Archimedes' law theory. We find excellent agreement, with the results of all the simulations falling very close to the predicted curve of ϕ *vs.* K_ϕ. We also examine the extreme case of frictionless spheres and find that, although no stagnant zone develops during penetration into such media, the value of their internal friction angle, $\phi = 9^\circ \pm 1^\circ$, also falls squarely on the theoretical curve. Finally, we use the modified Archimedes' law theory and an expression for the time-dependent growth of the stagnant zone to propose an explicit constitutive relation that fits excellently the force–depth curve throughout the entire penetration process.

Received 8th December 2018,
Accepted 1st March 2019

DOI: 10.1039/c8sm02480d

rsc.li/soft-matter-journal

1 Introduction

The ubiquity of granular materials (GMs) in nature and their significance to human society cannot be overstated. We interact on a daily basis with this form of matter: sand, gravel, cereals, powders, foodstuff, *etc.* An important aspect of granular science, which is far from fully understood, is the interaction of GMs with objects much larger than the grain size. Examples include animal and robotic locomotion in and on sand,[1,2] drilling in soil,[3,4] plowing,[5–7] and meteorite impacts.[8,9] The main difficulty in developing a fundamental understanding of this interaction is that GMs combine behaviours of solids and fluids, often simultaneously. This problem has been the focus of many studies and a canonical experiment consists of measuring forces on objects moving at a constant speed within GMs.[5,6,10–18] The resistance force of objects intruding GM quasistatically has been shown to follow the form[2,15,19–22]

$$F(z,v) = F_z(z) + F_v(z,v), \quad (1)$$

where $F_z(z)$ is a hydrostatic-like force that depends only on the penetration depth, z, and $F_v(z,v)$ is the reminiscent of viscosity, kicking in above a critical value v_c. Thus, investigations of $F_z(z)$ are often confined to the quasi-static regime $v < v_c$. Many experiments and simulations show that, at the steady state (see below) $F_z(z) = kz^\alpha$, but there is no consensus on the value of α. Hill *et al.*[23] and Peng *et al.*[24] found $\alpha = 1.3$ while Hou *et al.*,[25] Durian *et al.*,[12,19,26] and Lohse *et al.*[27] measured $\alpha = 1$ experimentally. Simulations by Xu *et al.*[16] also support $\alpha = 1.0$. Kang *et al.*[28] conducted an extensive range of experiments, all showing $\alpha = 1$, and went on to derive this value, using a continuum model.

The prefactor k was found to vary widely and be sensitive to the intruder geometry and granular medium. This makes k an important constitutive parameter and several attempts at modelling it exist in the literature. An empirical approach[29] fits the resistance force by decomposing the intruder's surface into many surface elements, measuring the force on each surface experimentally, and then summing them. A disadvantage of this approach is the large number of measurements required. Brzinski III *et al.*[12] proposed that $F_z(z) = C\mu\rho_g gAz$, with several

[a] *State Key Laboratory of Turbulence and Complex System, College of Engineering, Peking University, Beijing, 100871, China. E-mail: liucs@pku.edu.cn*
[b] *Imperial College London, London SW7 2BP, UK*
[c] *University of Cambridge, Cambridge CB3 0HE, UK*

values of C: 26 ± 3,[19] 15 ± 2,[12] and 35 ± 5,[26] all obtained by fitting experimental data. Askari and Kamrin[30] used a finite element method simulation to show that, in cohesionless media, frictional yielding underlies the resistive force.

Recently, Kang *et al.*[28] modelled the resistance force to quasi-static penetration, based on the Mohr–Coulomb criterion. They derived a linear relation between F_z and z, by considering only resistance forces normal to the intruder's surface, and established that the force follows a modified Archimedes' law, with the resistance proportional to the intruding volume. This modified Archimedes' law theory (MALT) made possible the derivation of several key results: (i) that k depends only on the internal friction angle ϕ; (ii) the explicit $k(\phi)$ relation; (iii) that the initial transient nonlinear part of the FDR is the result of the development of a stagnant zone ahead of the solid intruder.

We have three aims in this paper. The first is to use a range of discrete element method (DEM) simulations to investigate in detail the formation and growth dynamics of the SZ and the dependence of this process on medium properties. The second is to establish the dependence of the force–depth relation (FDR), and correspondingly the effective macroscopic internal friction angle, on a number of grain-scale properties, in particular, intergranular friction, grain size distribution and aspect ratio. The third aim is to investigate in greater detail the initial nonlinear regime of the FDR and relate it to the growth dynamics of the SZ.

The new results in this paper are the following. Firstly, we show, both numerically and experimentally, that what has been regarded in the literature so far as a single nonlinear pre-steady-state behaviour arises, in fact, from two distinctly different processes, resulting in different forms of the FDR. The first regime, A, involves direct material compression, while the second regime, B, involves plastic flow of the granular medium. We further find that the FDR in regime A is very sensitive to the inter-granular rolling friction, but that this parameter hardly affects regime B and the steady-state. In contrast, regime B and the steady state (C) are found to be sensitive to the initial packing fraction, the intergranular sliding friction, and the grain aspect ratio. We also find that the FDR is insensitive to the grain size, size distribution, and grain properties, such as density, shear modulus and coefficient of restitution (COR). Another significant result is that the SZ forms only at the beginning of the second regime, with the steady-state regime commencing when this development is complete. We then go on to determine the effective internal friction angles, ϕ, from the stress field in the simulated media. Measuring independently the gradient of the FDR in the steady state regime, K_ϕ, we show that all the simulated systems, as well as our experimental ones, satisfy very well the theoretical relation between K_ϕ and ϕ, derived by Kang *et al.*[28] Somewhat surprisingly, we find that a simulated system of frictionless spheres and water, in which no SZ develops, also falls squarely on the predicted K_ϕ–ϕ curve. Finally, we use the MALT to deduce the growth rate of the SZ and propose an explicit expression for the full FDR curve.

This paper is organised as follows. In Section 2, we describe the simulation method and system preparation. In Section 3, we carry out a comprehensive set of numerical simulations to investigate the dependence of the FDR on a number of grain-scale characteristics. In Section 4, we describe our experimental measurements of the resistance to penetration of cylinders into GM and compare those with the simulation results. This comparison provides a test of the reliability of the simulation method. In Section 5, we use our DEM data to quantify and visualise the velocity and stress fields in the GM and use these findings to test the theoretical model. In Section 6, we analyse the nonlinear part of the FDR and use the theoretical model to infer the dynamics of the growth of the SZ. We conclude with a discussion of our results and their ramifications in Section 7.

2 The numerical method

To test the modified Archimedes' law theory for object penetration into cohesionless granular matter, as well as the dynamics of growth of the SZ ahead of the intruding object, we carried out large-scale simulations, using the discrete element method (DEM).[31–33] In our context, the grains and the intruding object are the discrete elements, which interact *via* contact forces. The data consist of the time evolution of the grain positions, velocities, contact forces, and the drag forces experienced due to an effective viscous environment. We keep track of the normal, F_n, and tangential, F_t, components of both the elastic and viscous forces on each grain. For the contact forces, we adopt the Hertz–Mindlin (HM) model,[34] in which the inter-granular normal force is Hertzian[35] and the tangential force is based on the Mindlin–Deresiewicz model.[36] The tangential force includes the da Vinci–Amontons–Coulomb friction law, with μ the friction coefficient. The HM model includes a dissipative term determined by a constant coefficient of restitution (COR), e. In general, the COR depends on the collision relative velocity, which can be modelled by a viscoelastic contact model.[37–41] Nevertheless, both these models are employed commonly in DEM simulations.[17,34,42–44] In our simulations, the FDR is found to be completely independent of the COR (see Fig. 3h), making it prudent to use the HM model to study how the resistance force varies with e. Following Luding,[45] we model the rolling resistance as a torque $\boldsymbol{M}$ proportional to the normal contact force F_n and a rolling friction coefficient μ_r, but ignore the effects from the torsion resistance against the relative spin between grains. The specific expressions for various force components are given as follows:

$$F_n = k_n {\delta_n}^{3/2} + \gamma_n {\delta_n}^{1/4} u_n, \tag{2}$$

$$F_t = \begin{cases} k_t {\delta_n}^{1/2} \delta_t + \gamma_t {\delta_t}^{1/4} u_t & \text{if } |F_t| < \mu |F_n| \\ -\mu F_n \mathrm{sign}(u_t) & \text{if } |F_t| \geq \mu |F_n| \end{cases} \tag{3}$$

$$\boldsymbol{M} = -\mu_r F_n R_0 \boldsymbol{\omega}_0. \tag{4}$$

Here, δ_n and δ_t (u_n and u_t) are the normal and tangential components of the relative displacement (velocity) of the grain at the contact point, R_0 is the distance from the contact point to the mass centre of the grain, and $\boldsymbol{\omega}_0$ is the unit angular velocity vector of the object at the contact point. The parameters k_n, k_t, γ_n and γ_t are functions of the relative displacements δ_n and δ_t,

Table 1 The parameters in the simulated contact force model, with subscripts 'i' and 'g' denoting the intruder and grain parameters, respectively. $1/E = (1-\nu_g^2)/E_g$, $\lambda = \ln e/\sqrt{\ln^2 e + \pi^2}$, d_g and $m = \rho_g \pi d_g^3/6$ are the diameter and mass of each grain. μ_{gg} and μ_{gi} are the sliding friction coefficients between grains and between the grain and intruder, respectively. The rolling friction coefficients between grains and between the grain and intruder are both represented by μ_r

Parameter	Grain–grain interaction	Grain–intruder interaction
k_n	$\frac{E_g}{3(1-\nu_g^2)}\sqrt{d_g}$	$\frac{2\sqrt{2}}{3}E\sqrt{d_g}$
k_t	$\frac{2G_g}{2-\nu_g}\sqrt{d_g}$	$\frac{4\sqrt{2}G_g}{2-\nu_g}\sqrt{d_g}$
γ_n	$-\sqrt{\frac{5}{2}}\lambda\sqrt{mk_n}$	$-\sqrt{5}\lambda\sqrt{mk_n}$
γ_t	$-\sqrt{\frac{5}{3}}\lambda\sqrt{mk_t}$	$-\sqrt{\frac{10}{3}}\lambda\sqrt{mk_t}$
μ	μ_{gg}	μ_{gi}
μ_r	μ_r	μ_r

Young's modulus E, shear modulus G, Poisson's ratio ν, and COR e. These functions and all grain properties are given in Table 1.

A crucial choice in DEM simulations is the length of the time step: too large and the grains could move erratically, missing intergranular interactions; too small and simulating physically realistic times becomes impractical. For quasi-static simulations, a conventional choice is about 20% of the Rayleigh time step:[32] $T = \pi d_g(\rho_g/G_g)^{1/2}/(0.3262\nu_g + 1.7532)$, where d_g, ρ_g, G_g and ν_g are the particle's diameter, density, shear modulus, and Poisson ratio, respectively. The shear modulus was considered to have little effect on cone penetration[32] and we verified this assumption by studying explicitly the effects of shear moduli between 1 MPa and 1 GPa. Finding that changes in the shear modulus have indeed little to no effect on the resistance, we used a small value of 1 MPa in order to reduce the simulation time.

The simulated system is shown in Fig. 1. A cylinder, of height 150 mm and diameter D = 200 mm, contains granular matter up to a height of $H = 80 \pm 2$ mm. The number of grains

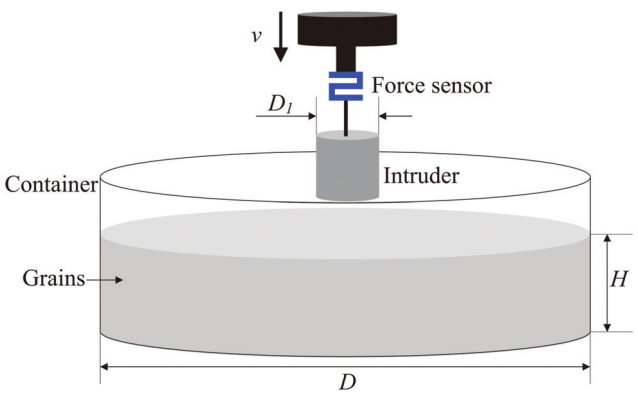

Fig. 1 Schematic representation of the simulated system and experimental system. A force sensor is connected between the intruder and the motor. The values of the parameters in the figure are as follows. In the experiment: D_1 = 5 cm, D = 45 cm, $H \approx$ 21 cm, v = 0.5 mm s^{-1}. In the simulations, D_1 = 3 cm, D = 20 cm, $H \approx$ 8 cm, v = 2 cm s^{-1}.

depends on their diameters, d_g: about 2.94×10^6 and 4.6×10^5 for d_g = 1.0 mm and d_g = 2.0 mm, respectively. A cylindrical intruder, of diameter 30 mm and length 50 mm, penetrates the granular medium quasi-statically at velocity $v < v_c$, where $v_c \approx \sqrt{2gd_g}/10$ is commonly taken as the upper limit for quasi-static penetration.[10] In this regime, the resistance force is independent of the velocity. For the grain sizes we used, d_g = 1.0 mm and 2.0 mm, v_c = 2.0 cm s^{-1} and 1.4 cm s^{-1}, respectively. We checked that the behaviour is the same for v = 1.0 cm s^{-1} and v = 2.0 cm s^{-1} (see below) and, to reduce simulation time, we used v = 2.0 cm s^{-1} for both grain sizes.

An initial simulation is run to prepare the initial state by dropping the grains into the container under gravity until they pile up to height H, forming about 2–3 grain layers above the bottom end of the stationary intruding cylinder. We then let the system equilibrate until its mean kinetic energy is less than 10^{-7} of the kinetic energy at the end of the dropping process. Once the initial state has been established, the intruder is driven down along the central axis at a constant speed v until it reaches a final depth of 3–4 cm.

3 The resistance force

It has been shown[2,18,26,28,44,46] that tangential forces on the intruder surface are negligible in this regime and the resistance force, F, is due to the total contribution of the normal forces against the intruder, as well as the forces on a granular SZ, which develops ahead of the intruder. It is convenient to define the dimensionless resistance and penetration depth:[28]

$$\tilde{p}_u \equiv \frac{F}{\rho_g \psi g S R}; \quad \tilde{h} \equiv \frac{h}{R}, \tag{5}$$

where ρ_g is the grain density, ψ the packing fraction, g the gravitational acceleration, $S = \pi R^2$ the intruder's section area, R the intruder's radius, and h the penetration depth. For brevity, we refer in the following to the non-dimensionalised variables $\tilde{p}_u$ and $\tilde{h}$ as resistance and penetration depth, respectively.

To ensure that the process is quasi-static, we checked the resistance numerically for penetration at v = 0.5, 1.0, and 2.0 cm s^{-1} into a medium with the properties specified in Table 2. The corresponding resistance–depth graphs, shown in Fig. 2, appear to collapse well up to fluctuations, for both the initial nonlinear and steady state linear regimes. The graphs also agree well with previous experimental results.[2,28,47]

Table 2 The material parameters used in the simulations in Fig. 2

Parameter	Value
Grain density, ρ_g	2500 kg m^{-3}
Grain diameter, d_g	1.0 mm
Friction coefficient, μ_{gg}	0.5
Friction coefficient, μ_{gi}	0.3
Rolling friction coefficient, μ_r	0.01
Grain shear modulus, G_g	1 MPa
Grain Poisson's ratio, ν_g	0.3
Grain aspect ratio, r	1.0
COR, e	0.8

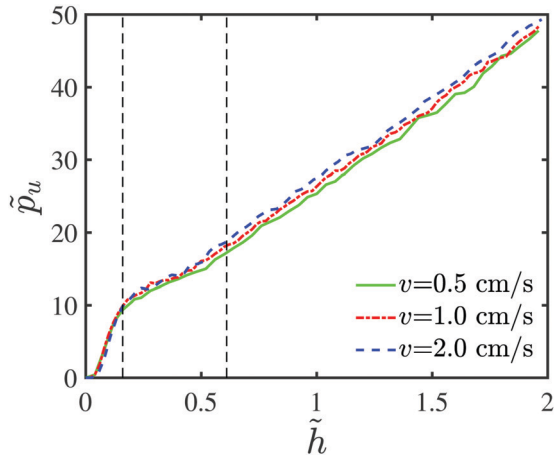

Fig. 2 The dimensionless resistance force dependence on the dimensionless penetration depth for penetration speeds: 0.5 cm s^{-1}, 1.0 cm s^{-1} and 2.0 cm s^{-1}. The left black dashed line is where boundary effects, due to the initial medium compaction, become negligible and the right black dashed line is where the SZ has almost reached its final size. The formation and growth of the SZ takes place between these lines, leading visibly to a different penetration dynamics.

Table 3 Fits of the linear regimes in Fig. 2

v (cm s^{-1})	K_ϕ	$\tilde{p}_0$	R-square
0.5	23.05	2.469	0.9981
1.0	22.86	3.619	0.9991
2.0	23.14	4.575	0.9987

We fitted the steady state regimes with $\tilde{p}_u = K_\phi \tilde{h} + \tilde{p}_0$. As shown in Table 3, we find that $K_\phi = 23.00 \pm 0.15$ for all three cases. The degree of the linear correlation is quantified by R-square, whose values are larger than 0.998 for all cases, establishing the high accuracy of the fits. Therefore, $v_c < 2$ cm s^{-1} is suitable for all systems and we use this speed in all our simulations.

Next, we carried out simulations to study the effects of media properties on the penetration dynamics and K_ϕ. We varied a number material parameters: initial packing fraction, sliding friction, rolling friction, shear modulus, grain sizes, and grain aspect ratios. In Fig. 3(a–f) we show the dependence of the force–depth relation (FDR) on several medium parameters as follows.

(a) In Fig. 3(a) we plot the dependence on the grain shear modulus. Shear moduli of most realistic grains are too large for DEM simulation and we adopted commonly used values: 10, 100, and 1000 MPa to test the effect of this parameter. The packing fraction of three simulations is 0.590 ± 0.002. We find that the plots are the same except that in assemblies of stiffer grains the fluctuations are somewhat larger. The fluctuations are due to disintegration of force chains in the medium causing grain rearrangements. Larger shear moduli allow for larger magnitude forces to build up along chains, leading to more violent chain breaks and hence larger local rearrangements.

(b) We find that the intergranular friction coefficient has a significant effect on $\tilde{p}_u$. Varying μ_{gg} gradually from 0.0 to 1.5 increases the normalised force consistently by more than an order of magnitude, as shown in Fig. 3(b). As expected, increasing the intergranular friction increases the internal friction angle[48] and consequently the gradient K_ϕ. Higher friction also leads to larger fluctuations, again, due to the breaking of locally stronger force chains causing larger local displacements.

(c) Interestingly, the rolling friction coefficient, μ_r, has no effect on the gradient K_ϕ. Boundary effects, however, persist deeper as μ_r is increased from 0.01 to 0.03. The reason is probably that the initial penetration involves compaction of the material

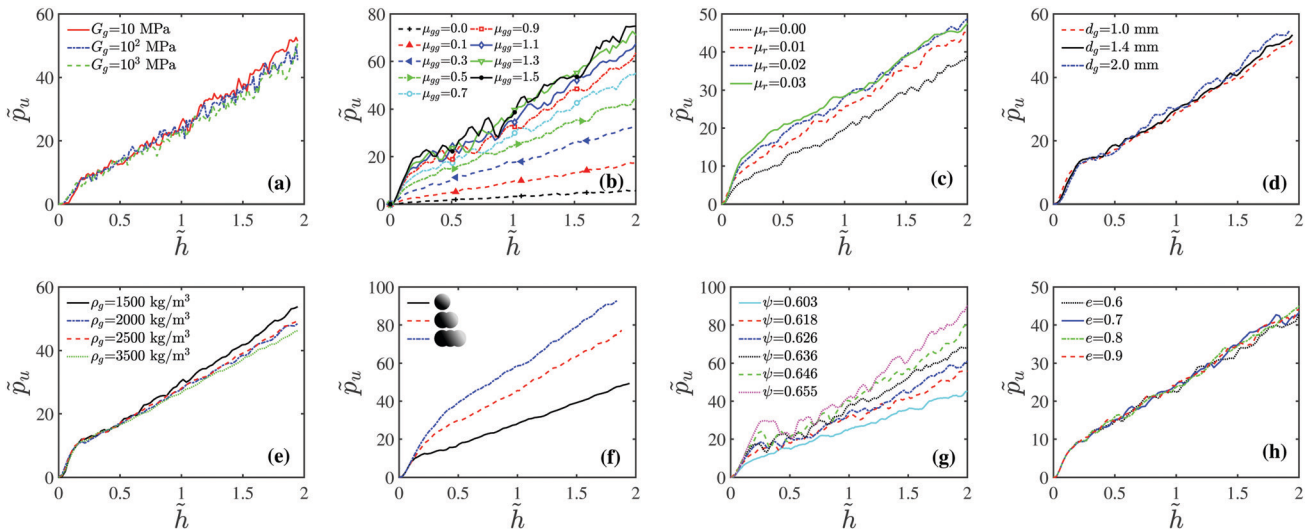

Fig. 3 The dependence of the force–depth relation on medium parameters. (a) The effect of shear modulus of grains for $\psi = 0.590 \pm 0.002$, $\mu_{gg} = 0.5$ and $d_g = 2$ mm; (b) the effect of the intergranular friction coefficient for $\psi = 0.603 \pm 0.001$ and $d_g = 2$ mm; (c) the effect of intergranular rolling friction for $\psi = 0.603 \pm 0.001$ and $\mu_{gg} = 0.5$; (d) the effect of grain size for $\psi = 0.632 \pm 0.003$ and $\mu_{gg} = 0.5$; (e) the effect of grain density for $\psi = 0.630 \pm 0.004$, $d_g = 1.0$ mm and $\mu_{gg} = 0.5$; (f) the effect of grain aspect ratio for $\psi = 0.630 \pm 0.003$ and $d_g = 1.0$ mm; (g) the effect of the packing fraction for $\mu_{gg} = 0.5$; (h) the effect of the COR for $\psi = 0.603 \pm 0.001$ and $\mu_{gg} = 0.5$.

ahead of the intruder and during this process grains are freer to rotate. The higher the rotational friction coefficient the higher the buildup of local torque moment on grains and consequently the larger the resistance force during this stage.

(d) We find that the normalised FDR, shown in Fig. 3(d), is insensitive at all to varying the grain size for the diameters we used: 1.0, 1.4 and 2.0 mm, at a packing fraction of 0.632 ± 0.003.

(e) We find a small effect of varying the grain density, ρ_g, shown in Fig. 3(e), with the resistance decreasing slightly as the density increases. This is the result of a competition between the smaller increase in the intergranular contact forces, which scale as $\sqrt{\rho_g}$ in eqn (2) and (3), and the normalisation of the resistance force by $1/\rho_g$, eqn (5).

(f) To test the effect of grain aspect ratio on the resistance force, we carried out simulations with two non-spherical types of grains: one consisting of two joined spheres, whose centres were 1/2 a diameter apart, giving a grain an aspect ratio of $r = 1.5$, and another of three linearly joined spheres, with their centres placed at half a diameter distances, giving a grain an aspect ratio of $r = 2$ (see the legend in Fig. 3(f)). The larger the aspect ratio the more difficult it is to rotate grains around a particular axis. As expected, this reduces the ability of the medium to yield and, consequently, increases significantly K_ϕ and the resistance force. We note that the mean coordination number also increases slightly with aspect ratio for the same packing fraction, which adds slightly to increase the resistance force.

(g) We vibrated the granular matter to obtain several initial packing fractions. As one would expect, varying the packing fraction, as shown in Fig. 3(g), also limits the mobility of grains, reducing the plastic flow around the intruder and consequently increases K_ϕ.

(h) Finally, it is shown in Fig. 3(h) that varying the COR, e, has no effect on the normalised FDR to within measurement error. This is because the process is quasistatic, whereas the COR is expected to affect mainly intergranular collisions. This observation has a useful implication for numerical simulations: it makes it possible to probe effects of packing fraction alone on an overall quasistatic response without changing any other macroscopic response simply by controlling the prepared initial packing fraction *via* the COR.

4 The experiment

To validate the reliability of the simulations and complement them, we carried out an experiment, whose setup is sketched in Fig. 1. It consisted of driving a 7 cm long cylinder, of diameter 5 cm, into a 21 cm deep assembly of 6 mm diameter spherical glass beads, packed within a cylindrical container of height 30 cm and diameter 45 cm. Before penetration, the granular medium was stirred thoroughly by hand and then flattened by passing a trowel across its surface in several directions. The trowel also had bubble levels, which enabled us to ensure that the surface was horizontal. The cylindrical intruder was initially inserted to a depth of about two grain diameters and then driven along the central axis of the container at a constant speed, $v = 0.5$ mm s^{-1}, which is sufficiently slow to ensure a quasi-static process. A sensor was used to record the resistance force during the intrusion at intervals of 0.05 s. The experiment was repeated five times to ensure reproducibility.

Table 4 The parameters in the simulation and experiment

Parameters	DEM, monodisperse	DEM, polydisperse	Experiment
Intruder diameter	5 cm	5 cm	5 cm
Grain diameter	6 mm	4.8–7.2 mm	6 ± 0.1 mm
Grain density	2500 kg m^{-3}	2500 kg m^{-3}	2500 kg m^{-3}
Packing fraction	0.575 ± 0.002	0.575 ± 0.002	0.575 ± 0.02
Sliding friction coefficient	0.5	0.5	0.5
Grain shear modulus	10 MPa	10 MPa	30 GPa
Rolling friction coefficient	0.02	0.02	—

To ensure that there are no crystallisation effects in the simulations, as well as to test the correspondence between the simulations and experiment, we simulated the experiment, using the same parameters, with both monodisperse and polydisperse grains, each repeated four times from different initial states. The simulated monodisperse grain diameters and the mean diameter of the polydisperse grains were also the same as in the experiment. For the polydisperse systems, we used a Gaussian diameter distribution, of mean 6 mm, standard deviation 0.3 mm and cutoffs at 4.8 mm $\leq d_g \leq$ 7.2 mm. In Table 4, we detail all the material parameters. During each simulation, we collected the resistance force and depth data, and plotted the normalised FDR, which we show in Fig. 4. It is evident from the plot that there is no discernible difference between the plots, indicating that the grain size distribution and the grain stiffness (which were different in the simulations, as discussed above) give the same results for the experiment and the simulations.

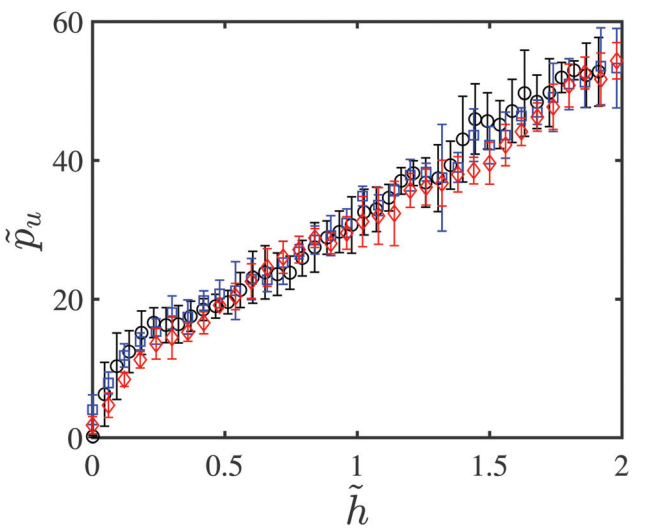

Fig. 4 The normalised FDRs in the experiments and simulations with both monodisperse and polydisperse grains: ○ – experiment; □ – simulation of monodisperse grains; ◊ – simulation of polydisperse grains. The error bars are the standard deviations over the four simulations and the five experiments, respectively.

This is also consistent with the evidence from Fig. 3(d). This substantiates the usefulness of our DEM simulations as a faithful description of the experiments we carried out.

5 Velocity and stress fields

The predictions in ref. 28 can be tested by visualising and analysing the penetration process and the response of the granular medium. In particular, most of the important information is in the velocity and stress fields around the intruder. The former can reveal how much of the material participates in the SZ, and the latter can show where the material is on the verge of yield. Simulations are useful for this purpose, enabling us to construct these fields in three dimensions.

The test simulations were carried out varying a range of different initial conditions and parameters. We vibrated the granular matter to obtain several initial packing fractions; we varied the intergranular sliding and rolling friction coefficients independently; we also varied the grains' shear modulus, mass density, and even simulated three different shapes. The large data set obtained from each simulation made it practical and convenient to coarse grain the velocity and stress fields first.

The coarse-graining comprises 'smearing' the fields within basic spherical volumes, of diameter $3d_g$, with a Gaussian coarse-graining function,[49,50]

$$\mathscr{W}(\boldsymbol{r}_i, \boldsymbol{r}) = \frac{1}{\left(\sqrt{2\pi}w\right)^3} \exp\left(-\frac{|\boldsymbol{r}_i - \boldsymbol{r}|^2}{2w^2}\right). \tag{6}$$

where $\boldsymbol{r}_i$, $\boldsymbol{r}$ and w are, respectively, the position of the ith grain, the centre of the basic sphere, and the smearing range. The coarse-grained velocity field is then

$$\boldsymbol{v}(\boldsymbol{r}) = \frac{\sum_{i=1}^{N} \boldsymbol{v}_i \times \mathscr{W}(\boldsymbol{r}_i, \boldsymbol{r})}{\sum_{i=1}^{N} \mathscr{W}(\boldsymbol{r}_i, \boldsymbol{r})} \tag{7}$$

where $\boldsymbol{v}_i$ is the velocity of the ith grain and N is the number of grains within the basic sphere.

The modified Archimedes' law theory (MALT)[28] is based on the Mohr–Coulomb yield criterion, which states that no plastic flow takes place if

$$\sin\phi > \kappa \equiv \frac{\sigma_1 - \sigma_3}{\sigma_1 + \sigma_3}, \tag{8}$$

where σ_1 and σ_3 are the large and small local principal stresses, respectively. To test the model we, therefore, need to compute the stress everywhere and visualise the spatial distribution of κ. We coarse-grained the stress tensor:

$$\boldsymbol{\sigma}(\boldsymbol{r}) = \frac{6}{\pi\left(3d_g\right)^3} \sum_{i,j \in V(\boldsymbol{r})} \boldsymbol{f}_{ij} \otimes \boldsymbol{r}_{ij}, \tag{9}$$

where $\boldsymbol{f}_{ij}$ and $\boldsymbol{r}_{ij}$ are, respectively, the force at and position vector of the contact between grains i and j, and the sum runs only over the contacts of grains contained fully within the basic sphere, whose centre is at $\boldsymbol{r}$. Solving for the eigenvalues of the stress tensor, we then obtained $\sigma_1(\boldsymbol{r})$, $\sigma_3(\boldsymbol{r})$ and κ. In Fig. 5(a and b), we show an example of the $||\boldsymbol{v}(\boldsymbol{r})||$ and κ fields during the penetration simulated for v = 2 cm s^{-1}, shown in Fig. 2.

To facilitate the MALT calculations, Kang *et al.*[28] presumed that ϕ is the same as the angle of repose. However, to establish this angle for the simulated grains not only requires additional extensive simulations, but those are also of little use because they cannot reproduce accurately the size and shape distributions of the experimental granular material. Additionally, since the simulations are quasistatic, then unavoidably $\kappa \leq \sin\phi$ everywhere. We therefore determined yielding regions in the simulations as follows. Firstly, we measured κ everywhere and recorded in each system at each time step. We then singled out the basic spheres in which $0.995\kappa_{\max} \leq \kappa \leq \kappa_{\max}$, and $\kappa_{\max}$ is its extreme value. The value of $\sin\phi$ was then defined as the average of κ over these regions. The incipient yield regions are shown (in yellow) in Fig. 5(b).

Fig. 5 and our experiments show clearly the three penetration regimes of the FDR. Regime A extends down to $\tilde{h} \approx 0.16 \equiv \tilde{h}_A$ and comprises a straightforward compaction of the material ahead of the intruder. It involves no flow away from the advancing path, as can be seen in the first row sub-figures of both Fig. 5(a and b). At the end of this stage, a small SZ starts forming as a result of the compression.

The process enters regime B, at $\tilde{h}_A$, when the yielded material is forced away from the advancing path, generating a flow that can be observed clearly in the second row sub-figures in Fig. 5(a) at $\tilde{h}$ = 0.24 and 0.373. During this stage, the SZ grows steadily, as seen clearly in Fig. 5. The velocity field shows that the SZ is roughly conical (Fig. 5(a)), but the shear bands between the boundary of the SZ and the flowing medium distort this shape somewhat.[51] The growing SZ affects noticeably the FDR up to about $\tilde{h} \approx 0.61 \equiv \tilde{h}_B$. This increase is slower than during either of regimes A and the third one, C. Below, we relate this increase directly to the growth rate of the SZ. The distinction between regimes B and C was not recognised in ref. 28, but this can be observed in their data, *e.g.* their Fig. 2(f).

Regime C commences, in principle, once the SZ has reached a limit shape. Beyond this point, the force increases linearly, which reflects in the MALT the fact that the effective volume of the intruder, which consists of both the intruding object and the SZ, has reached a maximal limiting value.[28] While Fig. 2 suggests that $\tilde{h}_B \approx 0.61$, the stress field shown in Fig. 5(b) continues to evolve somewhat beyond this point, showing a further growth of the SZ beyond $\tilde{h}_B$. However, this additional growth cannot be observed in Fig. 2, indicating that it is too small to affect the resistance force appreciably.

As can be observed in Fig. 3, the buildup of the SZ and its growth depend on the intergranular sliding friction. No evidence of any SZ formation can be observed in simulations of frictionless grains (see Fig. 6) and indeed no regime B appears in the corresponding FDR, supporting our conceptual understanding of regime B. This also agrees well with the FDR for frictionless spheres, shown in Fig. 3(b).

It has been shown that the steady-state gradient, $K_\phi = \mathrm{d}\tilde{p}_u/\mathrm{d}\tilde{h}|_{\tilde{h}>\tilde{h}_B}$, is a constitutive property of the granular material, depending only on the value of ϕ,[28]

$$K_\phi = \frac{2(1+\sin\phi)}{1-\sin\phi} \mathrm{e}^{\pi\tan\phi} \int_0^1 \eta A(\eta, \phi) \mathrm{d}\eta, \tag{10}$$

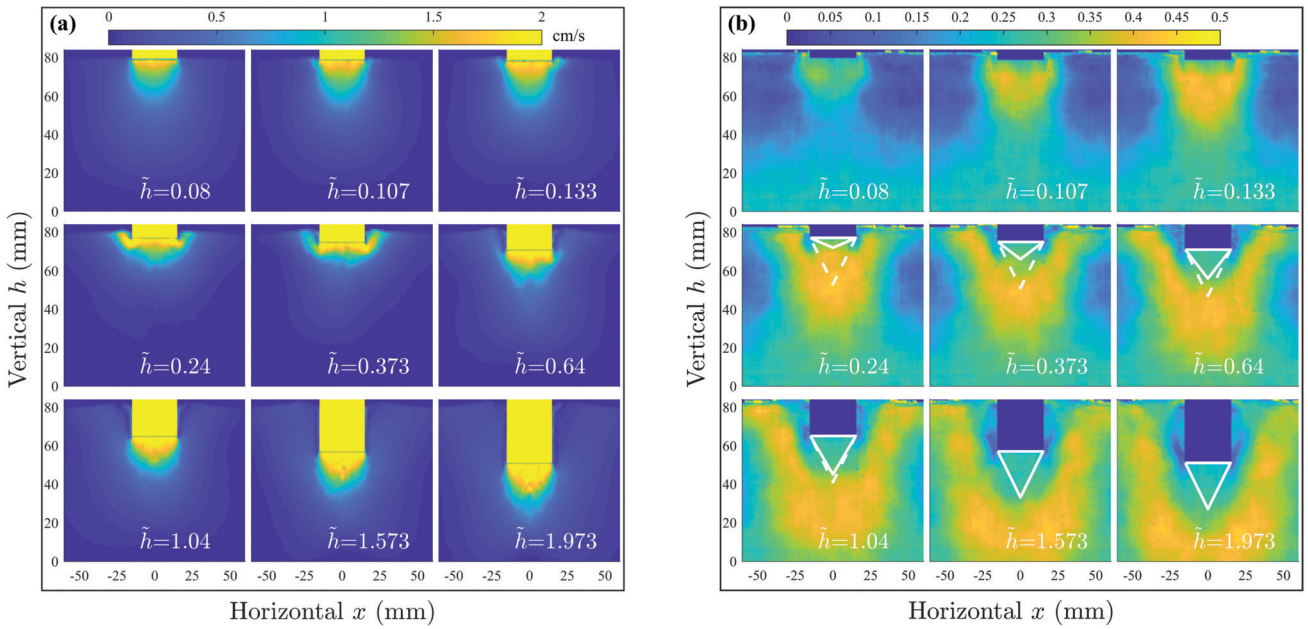

Fig. 5 The evolutions of: (a) the velocity ($\|\boldsymbol{v}(\boldsymbol{r})\|$) field and (b) the stress (κ) field in the GM with penetration depth, during the simulation at v = 2 cm s^{-1} in Fig. 2. The dashed and solid lines in (b) are the final and temporal boundaries of the SZ, respectively. Both the temporal and final boundaries are determined by the value of κ, derived from the stress field. The final boundaries are approximated as an isosceles triangle, of apex angle ($\pi/2 - \phi$), where ϕ is determined by the value of κ in regime C, as detailed in the main text. The temporal boundaries are drawn as an isosceles triangle, whose apex is where the value of κ is 0.75 sin ϕ.

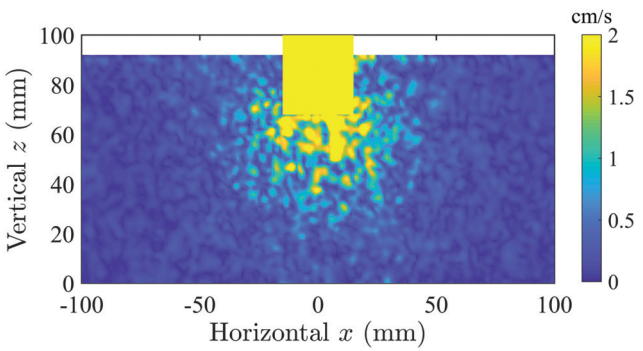

Fig. 6 The velocity field for frictionless spheres at penetration depth $\tilde{h}$ = 1.6.

where $A(\eta,\phi) = \left(\frac{r_1^{1+\tan^2\beta}}{r_2^{\tan^2\beta} r_3}\right)^{\sin\phi} e^{\sin\phi \tan\beta Z(\eta,\phi)}$. The quantities β, r_1, r_2, r_3 and $Z(\eta,\phi)$ can be computed as

$$\begin{cases} \beta = \pi/4 - \phi/2, \\ r_1 = R\left(1 + \dfrac{2(1-\eta)}{\tan\beta} e^{\frac{\pi}{2}\tan\phi}\right), \\ r_2 = R\left(1 + \dfrac{(1-\eta)}{\tan\beta} e^{\frac{\pi}{2}\tan\phi}\right), \\ r_3 = R\eta, \\ Z = \displaystyle\int_0^{\pi/2} \frac{-(1-\eta)e^{\theta\tan\phi}\cos(\theta+\beta)}{\cos\phi[\sin\beta + (1-\eta)e^{\theta\tan\phi}\sin(\theta-\beta)]} d\theta. \end{cases} \quad (11)$$

The predicted dependence of K_ϕ on ϕ, which is shown in Fig. 7 (solid line), has been supported by experimental results in the literature.[2,26,28]

This allows us to calculate ϕ in terms of the κ-field, obtained from DEM results, then find K_ϕ, by fitting the steady state regime in the corresponding FDR, construct a scatter plot of those in the ϕ–K_ϕ plane, and test the level of agreement with

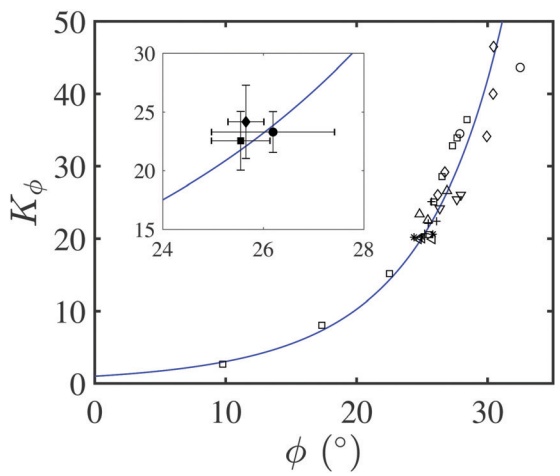

Fig. 7 A scatter plot of the experimental and simulated results in the ϕ–K_ϕ plane. Δ (G), □ (μ), * (μ_r), ∇ (d_g), + (ρ_g), ○ (r), ◊ (ϕ) and ◁ (e) are obtained from the DEM simulations of Fig. 3(a–h), respectively. The solid symbols and error bars in the inset are for the systems shown in Fig. 4: ■ (monodisperse grains), ● (polydisperse grains) and ♦ (experiment grains). The error bars are the standard deviations over the four simulations and the five experiments, respectively. All the results fall nicely on the theoretical relation, eqn (10), shown as a solid line.

the theoretical curve. For this test, we use the DEM results of the systems shown in Fig. 3, each of which is represented by a point, (ϕ,K_ϕ), in Fig. 7. The points collapse very nicely on the theoretical curve. We have further checked the values of ϕ and K_ϕ for the experiments and simulations with both monodisperse and polydisperse grains, which we show in Fig. 4. These points are plotted in the inset of Fig. 7, and they are also consistent with the theoretical prediction.

Fig. 7, which summarises all our experimental and numerical observations, not only supports well the MALT for cohesionless dry GM but it also shows the high sensitivity to intergranular sliding friction, packing fraction and grain shapes, and the low sensitivity to grain sizes, density, shear modulus, rolling friction and COR. Interestingly, the system of frictionless spheres, which develops no SZ, exhibits a finite value of ϕ, albeit the lowest of all the simulated systems. It should also be noted that the theoretical curve converges to $K_\phi = 1$ when $\phi = 0$, which corresponds to water. In this sense, the theoretical relation (10) bridges between these two different types of fluids.

6 The nonlinear FDR regime and SZ growth

Next, we focus on the two transient nonlinear regimes, preceding the steady state behaviour, which we observe in both our experiments and simulations. The MALT relates the FDR directly with the growth of the SZ through the relation[28]

$$\tilde{p}_\mathrm{u} = K_\phi\left(\frac{V(\tilde{h})}{\pi R^3}+\tilde{h}\right), \tag{12}$$

where $V(\tilde{h})$ in the first term on the right hand side is the increasing volume of the granular SZ, which advances ahead of the solid intruder, and the second term is due to the steady increase in the volume of our solid cylinder, as it enters the medium. The growth of the SZ, $\mathrm{d}V/\mathrm{d}\tilde{h} > 0$, should lead to a super-linear form of the FDR, during the transient regime. This is at odds with the original observation in ref. 28, in which the gradient of the FDR appeared to start high and decrease until settling into the steady state value K_ϕ in regime C.

Our observations explain this discrepancy: the SZ does not form before the beginning of regime B and it is only from that regime onward that the MALT applies. The rapid force increase in regime A is simply a consequence of straightforward material compression. The apparent sub-linear increase over the entire initial penetration is caused by the smaller overall increase in regime B, which is a result of the initial very low gradient in this regime – much lower than either A or C. This new understanding allows us to deduce the growth rate of the SZ, $V(\tilde{h})$, from the FDR.

The rate of growth of $V(\tilde{h})$ must be sub-linear because the volume eventually converges to a steady-state value. For simplicity, we model the SZ as a perfect cone, whose base coincides with the bottom of the intruding cylinder and its apex extends by a (non-dimensionalised) distance $\tilde{H} = H/R$ into the granular material. The cone volume is $V(\tilde{h}) = \pi R^3\tilde{H}/3$, with $\tilde{H}$ increasing from zero at $\tilde{h}_\mathrm{A}$ (end of regime A) to $\tilde{H}_\mathrm{ss}$ at $\tilde{h}_\mathrm{B}$ (end of regime B). Following observations from the observed FDRs, we take the initial gradient to be $\mathrm{d}\tilde{H}/\mathrm{d}\tilde{h} = 0$ at $\tilde{h}_\mathrm{A}$ (see, *e.g.* Fig. 3(b, d, g) and 4). One could argue that this value may be slightly higher in other systems, but our next analysis can be readily adjusted accordingly, if this turns out to be the case. We use the Mohr–Coulomb criterion for the final, steady-state, value of the cone angle: $2\beta = \pi/2 - \phi$, which gives $\tilde{H}_\mathrm{ss} = \tan(\pi/4 + \phi/2)$. To accommodate both the initial gradient and the convergence to steady state, we propose the form

$$\tilde{H} = \tilde{H}_\mathrm{ss}\left[1-\mathrm{e}^{-\left(\frac{\tilde{h}-\tilde{h}_\mathrm{A}}{\tilde{h}_\mathrm{B}-\tilde{h}_\mathrm{A}}\right)^2}\right]. \tag{13}$$

This form, combined with eqn (12), describes the behaviour in regime B. Specifically, for $\tilde{h}_\mathrm{A} < \tilde{h} < \tilde{h}_\mathrm{B}$,

$$\frac{\mathrm{d}\tilde{p}_u}{\mathrm{d}\tilde{h}} = \frac{2K_\phi\tilde{H}_\mathrm{ss}\left(\tilde{h}-\tilde{h}_\mathrm{A}\right)\mathrm{e}^{-\left(\frac{\tilde{h}-\tilde{h}_\mathrm{A}}{\tilde{h}_\mathrm{B}-\tilde{h}_\mathrm{A}}\right)^2}}{3\left(\tilde{h}_\mathrm{B}-\tilde{h}_\mathrm{A}\right)^2} \equiv f(\tilde{h}) \tag{14}$$

It is useful to fit the entire FDR with one analytic expression. This requires smoothing the crossovers between the regimes. To this end, we define a smoothing function, to be applied at both $\tilde{h}_\mathrm{A}$ and $\tilde{h}_\mathrm{B}$:

$$G(a,b,\tilde{h}_0,\Delta) = \frac{b+a}{2}+\frac{b-a}{2}\tanh\left(\frac{\tilde{h}-\tilde{h}_0}{\Delta}\right). \tag{15}$$

where Δ is a (non-dimensional) lengthscale that is much shorter than either $\tilde{h}_\mathrm{A}$ or $\tilde{h}_\mathrm{B} - \tilde{h}_\mathrm{A}$ and a and b are the functional forms of $\mathrm{d}\tilde{p}_\mathrm{u}/\mathrm{d}\tilde{h}$ far below (compared to Δ) and far above the crossover point $\tilde{h}_0$. The FDR can now be fitted as

$$\frac{\mathrm{d}\tilde{p}_\mathrm{u}}{\mathrm{d}\tilde{h}} = \begin{cases} G\left(K_\mathrm{A}, f(\tilde{h}), \tilde{h}_\mathrm{A}, \Delta\right) & 0 \le \tilde{h} < \dfrac{\tilde{h}_\mathrm{A}+\tilde{h}_\mathrm{B}}{2} \\ G\left(f(\tilde{h}), K_\phi, \tilde{h}_\mathrm{B}, \Delta\right) & \tilde{h} \ge \dfrac{\tilde{h}_\mathrm{A}+\tilde{h}_\mathrm{B}}{2} \end{cases} \tag{16}$$

Note that, by construction, the two gradients match at $(\tilde{h}_\mathrm{A} + \tilde{h}_\mathrm{B})/2$. All the parameters of this generalised relation can be read off directly from the FDR. Even the crossover scale, Δ, can be chosen by comparison to $\tilde{h}_\mathrm{A}$ and $\tilde{h}_\mathrm{B} - \tilde{h}_\mathrm{A}$.

Integrating (16) numerically, we obtain an excellent fit for the entire FDR curve in all the experiments and simulations.

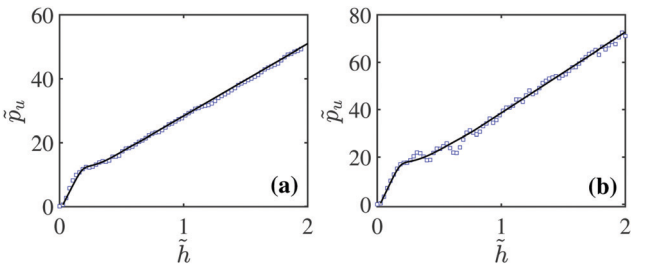

Fig. 8 Examples of the unified fit for the entire FDR: (a) the system in Fig. 2 (v = 2.0 cm s^{-1}), in which $\tilde{h}_\mathrm{A}$ = 0.16 and $\tilde{h}_\mathrm{B}$ = 0.61; (b) the system in Fig. 3(b) (μ = 1.1), in which $\tilde{h}_\mathrm{A}$ = 0.16 and $\tilde{h}_\mathrm{B}$ = 0.72. The squares and solid line represent, respectively, the DEM simulation data and the fitting curve obtained by integrating eqn (16).

The fit quality is demonstrated for two example systems, shown in Fig. 2, for $v = 2.0$ cm s^{-1}, and in Fig. 3(b), for $\mu = 1.1$ (Fig. 8).

7 Conclusions

To conclude, we carried out a wide range of simulations and a set of supporting experiments. We showed that quasi-static penetration of a cylindrical object into granular materials proceeds in three regimes, observed clearly in the force–depth relation (FDR). The first, regime A, is short and involves an initial compression of the material immediately ahead of the intruder. This compression leads to a sharp, roughly linear, increase of the FDR. During the second regime, B, the intruder squeezes the material away from its path. This is facilitated by a buildup of a dense cone-like stagnant zone (SZ), which pushes the material sideways by its inclined surface. Regime B continues until the SZ reaches a final size. The nonlinearity of the FDR in this regime is explained by the recently derived modified Archimedes' law theory (MALT),[28] eqn (12), as the result of the growth of the SZ. Once the SZ has reached its largest size, the penetration converges to a steady-state process, regime C, and can continue, in principle, as long as the system boundary and cylinder length allow. The FDR is linear in this regime, supporting the MALT prediction of $\alpha = 1$. The gradient, K_ϕ, of the terminal linear increase depends only on the internal friction angle, ϕ.[28]

This behaviour is consistent in all the simulations we conducted, in which we varied the initial packing fraction, inter-grain sliding and rolling friction coefficients, grains' shear modulus, density, coefficient of restitution, size distribution (monodisperse and same-mean Gaussian), and shape (spheres, double-spheres and triple-spheres). The only exception to this general behaviour is a medium made of frictionless spheres, in which we observed no SZ buildup (Fig. 6). Correspondingly, this system also exhibits no regime B in the FDR.

The value of K_ϕ was found to be sensitive to the inter-grain sliding friction, initial packing fraction and grain shape. It was hardly affected at all by the grains' size, size distribution, shear modulus, COR, and density. The rolling friction coefficient was found to affect only the duration of regime A. We mapped the velocity and deviatoric stress fields from the simulation data and determined from the latter the internal friction angle ϕ. Using this value and the observed values of K_ϕ, we constructed a scatter plot in the plane ϕ–K_ϕ. We find that, in spite of the sensitivity to granular characteristics, all the points in the scatter plot collapse very well on top of the theoretical curve, derived by Kang *et al.*[28]

Of some interest is the system of frictionless spheres, which need not necessarily behave like those of frictional grains. Indeed, we have observed that the absence of friction prohibits the development of a SZ, which agrees with the absence of the B regime in its FDR. Nevertheless, using our method, we determined the effective internal friction angle of this system from the κ-field: $\phi = 9^\circ \pm 1^\circ$. Unsurprisingly, this value is lower than that of any of the other systems we studied. Reading off the value K_ϕ from its FDR, we have shown that this system also falls on top of the theoretical $K_\phi(\phi)$ curve, demonstrating the applicability of the MALT to this singular case as well. Moreover, eqn (10) gives $K_\phi(\phi = 0) = 1$, which is the expectation from the traditional Archimedes' law for solids penetrating Newtonian liquids. This suggests that relation (10) appears to bridge between the descriptions of the seemingly different media of conventional liquids and GMs.

Finally, we used our observations of the nonlinearity in stage B of the FDR to deduce the rate of volume increase of the SZ with depth. This expression was then used to construct an explicit expression that fits the entire FDR curve and can be used as the constitutive description of the described penetration process.

Conflicts of interest

There are no conflicts of interest to declare.

Acknowledgements

YF and CL acknowledge gratefully support from the National Natural Science Foundation of China under project 11472011. RB acknowledges the hospitality of the State Key Laboratory of Turbulence and Complex System, College of Engineering, Peking University, where this work was done.

References

1 C. Li, T. Zhang and D. I. Goldman, *Science*, 2013, **339**, 1408–1412.
2 J. Aguilar and D. I. Goldman, *Nat. Phys.*, 2016, **12**, 278–283.
3 L. J. Munkholm, P. Schjonning, K. J. Rasmussen and K. Tanderup, *Soil Tillage Res.*, 2003, **71**, 163–173.
4 Q. Xue, H. Leung, R. Wang, B. Liu, L. Huang and S. Guo, *Nonlinear Dyn.*, 2015, **83**, 2003–2018.
5 N. Gravish, P. B. Umbanhowar and D. I. Goldman, *Phys. Rev. Lett.*, 2010, **105**, 128301.
6 B. Percier, S. Manneville, J. N. Mcelwaine, S. W. Morris and N. Taberlet, *Phys. Rev. E: Stat., Nonlinear, Soft Matter Phys.*, 2011, **84**, 51302.
7 N. Gravish, P. B. Umbanhowar and D. I. Goldman, *Phys. Rev. E: Stat., Nonlinear, Soft Matter Phys.*, 2014, **89**, 042202.
8 H. J. Melosh, *Research supported by NASA*, Oxford University Press (Oxford Monographs on Geology and Geophysics, No. 11), New York, 1989, vol. **11**, p. 253.
9 K. Holsapple, *Annu. Rev. Earth Planet. Sci.*, 1993, **21**, 333–373.
10 R. Albert, M. Pfeifer, A. L. Barabasi and P. Schiffer, *Phys. Rev. Lett.*, 1999, **82**, 205–208.
11 I. Albert, P. Tegzes, B. Kahng, R. Albert, J. G. Sample, M. Pfeifer, A. L. Barabasi, T. Vicsek and P. Schiffer, *Phys. Rev. Lett.*, 1999, **84**, 5122.
12 T. A. Brzinski and D. J. Durian, *Soft Matter*, 2010, **6**, 3038–3043.
13 D. J. Costantino, J. Bartell, K. Scheidler and P. Schiffer, *Phys. Rev. E: Stat., Nonlinear, Soft Matter Phys.*, 2011, **83**, 11305.

14 F. Guillard, Y. Forterre and O. Pouliquen, *Phys. Rev. Lett.*, 2013, **110**, 138303.
15 M. Tiwari, T. R. Mohan and S. Sen, *Phys. Rev. E: Stat., Nonlinear, Soft Matter Phys.*, 2014, **90**, 62202.
16 Y. Xu, J. T. Padding and J. A. M. Kuipers, *Phys. Rev. E: Stat., Nonlinear, Soft Matter Phys.*, 2014, **90**, 62203.
17 F. Guillard, Y. Forterre and O. Pouliquen, *Phys. Rev. E: Stat., Nonlinear, Soft Matter Phys.*, 2015, **91**, 22201.
18 X. Zhang, D. Sheng, G. P. Kouretzis, K. Krabbenhoft and S. W. Sloan, *Phys. Rev. E: Stat., Nonlinear, Soft Matter Phys.*, 2015, **91**, 22204.
19 H. Katsuragi and D. J. Durian, *Nat. Phys.*, 2007, **3**, 420.
20 D. I. Goldman and P. B. Umbanhowar, *Phys. Rev. E: Stat., Nonlinear, Soft Matter Phys.*, 2007, **77**, 21308.
21 A. H. Clark, L. Kondic and R. P. Behringer, *Phys. Rev. Lett.*, 2012, **109**, 238302.
22 A. Seguin, Y. Bertho, P. Gondret and J. Crassous, *EPL*, 2009, **88**, 44002.
23 G. Hill, S. Yeung and S. A. Koehler, *EPL*, 2005, **72**, 137.
24 Z. Peng, X. Xu, K. Lu and M. Hou, *Phys. Rev. E: Stat., Nonlinear, Soft Matter Phys.*, 2009, **80**, 21301.
25 M. Hou, Z. Peng, R. Liu, Y. Wu, Y. Tian, K. Lu and C. K. Chan, *Sci. Technol. Adv. Mater.*, 2005, **6**, 855.
26 T. A. Brzinski III, P. Mayor and D. J. Durian, *Phys. Rev. Lett.*, 2013, **111**, 168002.
27 D. Lohse, R. Rauhe, R. Bergmann and D. V. Der Meer, *Nature*, 2004, **432**, 689.
28 W. Kang, Y. Feng, C. Liu and R. Blumenfeld, *Nat. Commun.*, 2018, **9**, 1101.
29 C. Li, T. Zhang and D. I. Goldman, *Science*, 2013, **339**, 1408–1412.
30 H. Askari and K. Kamrin, *Nat. Mater.*, 2016, **15**, 1274.
31 P. A. Cundall and O. D. Strack, *Geotechnique*, 1979, **29**, 47–65.
32 M. Paulick, M. Morgeneyer and A. Kwade, *Powder Technol.*, 2015, **283**, 66–76.
33 Y. Guo and J. S. Curtis, *Annu. Rev. Fluid Mech.*, 2015, **47**, 21–46.
34 Y. Tsuji, T. Tanaka and T. Ishida, *Powder Technol.*, 1992, **71**, 239–250.
35 H. R. Hertz, *Verhandlung des Vereins zur Beforderung des GewerbefleiBes*, Berlin, 1882, p. 449.
36 R. D. Mindlin, *J. Appl. Mech.*, 1953, **20**, 327–344.
37 G. Kuwabara and K. Kono, *Jpn. J. Appl. Phys.*, 1987, **26**, 1230.
38 N. V. Brilliantov, F. Spahn, J.-M. Hertzsch and T. Pöschel, *Phys. Rev. E: Stat., Nonlinear, Soft Matter Phys.*, 1996, **53**, 5382.
39 F. G. Bridges, A. Hatzes and D. Lin, *Nature*, 1984, **309**, 333.
40 G. LoCurto, X. Zhang, V. Zakirov, R. Bucklin, L. Vu-Quoc, D. Hanes and O. Walton, *Trans. ASAE*, 1997, **40**, 789–794.
41 D. Ma and C. Liu, *J. Appl. Mech.*, 2015, **82**, 121006.
42 S. Luding, E. Clément, A. Blumen, J. Rajchenbach and J. Duran, *Phys. Rev. E: Stat., Nonlinear, Soft Matter Phys.*, 1994, **50**, 4113.
43 S. Fazekas, J. Török and J. Kertész, *Phys. Rev. E: Stat., Nonlinear, Soft Matter Phys.*, 2007, **75**, 011302.
44 F. Zhou, S. G. Advani and E. D. Wetzel, *Phys. Fluids*, 2007, **19**, 013301.
45 S. Luding, *Granular Matter*, 2008, **10**, 235.
46 C. H. Trautmann and T. D. Orourke, *J. Geotech. Eng.*, 1985, **111**, 1077–1092.
47 W. Jung, S. M. Choi, W. Kim and H.-Y. Kim, *Phys. Fluids*, 2017, **29**, 041702.
48 J. Horabik and M. Molenda, *Biosyst. Eng.*, 2016, **147**, 206–225.
49 I. Goldhirsch, *Granular Matter*, 2010, **12**, 239–252.
50 B. Andreotti, Y. Forterre and O. Pouliquen, *Granular media: between fluid and solid*, Cambridge University Press, 2013.
51 M. Harrington, H. Xiao and D. J. Durian, 2018, arXiv preprint arXiv: 1812.08227.